Permeability and mechanical integrity of porous biomorphic SiC ceramics for application as hot-gas filters

A. Gómez-Martín[1,2], M. P. Orihuela[1-3], J. A. Becerra[3], J. Martínez-Fernández[1,2], J. Ramírez-Rico[1,2,*]

[1] Dpto. Física de la Materia Condensada, Universidad de Sevilla, Avda. Reina Mercedes SN, 41012 Sevilla, Spain.
[2] Instituto de Ciencia de Materiales de Sevilla (CSIC-Univ. Sevilla), Avda. Américo Vespucio 49, 41092 Sevilla, Spain.
[3] Dpto. de Ingeniería Energética, Universidad de Sevilla, Camino de los Descubrimientos SN, 41092 Sevilla, Spain.
[*] Corresponding author. Tel. +34 954550963, email: jrr@us.es

ABSTRACT

Biomorphic SiC is a biotemplated material fabricated by Si melt-infiltration of carbon preforms from wood pyrolysis. In this work, porous bioSiC ceramics from five different wood precursors, with porosities between 45 and 72% were studied for their feasibility in filtering applications.

Gas permeability and mechanical stability were investigated as a function of the microstructure of the starting wood precursor. Air-permeation performance at room temperature was measured for a range of flow rates, and the permeability constants were assessed by fitting of Forchheimer's equation to the experimental data. Darcian permeabilities were achieved in the range 10^{-11}-10^{-12} m^2, while inertial terms were in the range 10^{-7}-10^{-8} m, showing a correlation with the average pore size and orientation of the larger channels. Regarding the mechanical stability, maximum compressive strength values were reached in the range of 3-115 MPa.

These results improve our understanding of the ways in which the microstructure influences permeability and mechanical robustness, enabling the device requirements to be tailored by selecting the wood precursor. It was also shown that these materials are promising for hot-gas filtering applications.

1 Introduction

Owing to their potential properties, porous ceramic materials have been of increasing interest for many advanced applications such as filter materials [1, 2], catalyst carriers [3], heat exchangers [4], thermal insulators [5], and biomedical implants [6, 7]. Recently, applications in various fields for separation filters have become important in reducing environmental pollution. In diesel engines, particulate matter (PM) is generated as a result of incomplete combustion and released into the environment [8]. These particles have been shown to have harmful effects on health and ecosystems [9, 10], so that their emission is now restricted by new regulations [11]. Not only is the total mass of emitted particles restricted but also their number, taking into account the impact of the smallest particles which, despite representing a small fraction of the total mass emitted, are now being identified as the most harmful.

The imposition of additional limits on the number of soot particles requires the development and improvement of after-treatment systems. One of the solutions is the use of diesel particulate filters (DPF) as physical barriers that remove particles from the exhaust gas of a diesel engine [12]. The most widely used filters to reduce the solid emissions is the well-known *wall flow filter*. This type of filter normally consists of a porous ceramic material with a honeycomb structure designed to remove solid particles from a gas flow [13]. Ceramic materials are effective for this application because of their thermomechanical and chemical stability, especially at high temperatures. Materials such as silicon carbide, cordierite, mullite, aluminum titanate, and silicon nitride are used as substrates, though the most commonly used are made of silicon carbide and cordierite because of their superior properties [14]. Of these two materials, silicon carbide has increased in popularity owing to its high melting temperature, good heat-transfer capability, low coefficient of thermal expansion, excellent resistance to oxidation and corrosion, and high hardness and strength [15]. All these properties make SiC a promising material to use as a filter, but its use is limited due to the high manufacturing cost [13].

An advantageous method for manufacturing ceramic materials that would avoid current problems in the use of SiC as a filter is called the *replica technique*, which uses a synthetic or natural porous precursor as a pattern. This pattern is reacted with a secondary phase to yield a porous ceramic material that mimics the original template microstructure [16, 17]. Biomorphic silicon carbide (bioSiC) is a SiC-based material fabricated by this low-cost and environmentally friendly process [18-20]. In this case, the method consists of a reactive infiltration of molten silicon by capillarity into a carbon preform made by high-temperature pyrolysis of a porous precursor [21]. After the infiltration process a SiC/Si composite is created with its pores totally or partially filled with residual silicon, depending on the carbon preform pore distribution. Then, the excess silicon can be removed by chemical etching or other methods to produce a porous silicon carbide material that replicates the microstructure of the original precursor

with high interconnected porosity elongated along the tree-growth direction [22]. This manufacturing process for SiC has several advantages compared to traditional techniques [16]: lower processing temperatures, faster fabrication, additives being unnecessary, and complex shapes being easy by machining the carbon preform. The outstanding advantage over other manufacturing methods is that the final properties of the material, such as total porosity and pore-size distribution, can be adjusted by the choice of the original precursor, whether of wood or recycled wood products, which provide a large range of possible pore distributions [23].

The feasibility of porous bioSiC ceramics as filters in gasification plants has been evaluated in previous works [24, 25]. Because of its controllable microstructure that originates from the precursor, interconnected porosity and low processing cost, bioSiC could also be promising as a particulate filter in diesel engines. For filtration applications, the permeability is one of the most important properties because it is directly related to pressure loss [13]. Recent studies have been conducted on many ceramic materials to determine their permeability and to assess the influence of their microstructure on the resulting pressure drop and efficiency [1, 26]. These parameters have been demonstrated to depend on volume fraction of porosity as a first approximation, but also on pore size and connectivity [27]. If the permeability is known as a function of the microstructure, then the pressure drop can be predicted under a given flow rate and the microstructure can be improved by tailoring pore characteristics [28]. However, high values of porosity cause lower mechanical strength and stability [22-24], despite the high permeability [29], and thus finding the balance between the two parameters is one of the main challenges in making a suitable material for filtering applications.

This work examines the viability of SiC synthesized by silicon melt infiltration of carbon preforms from wood precursors as hot-gas filter materials, with the aim of gaining a fuller understanding of microstructure and device requirements. A complete microstructural characterization was made of porous bioSiC ceramics from five different wood precursors, including four natural woods and one recycled wood product. The influence of some microstructural parameters (such as volume fraction of porosity, pore-size distribution, tortuosity, and orientation) on gas permeability and mechanical stability is discussed. Based on the experimental values of these properties, the suitability of this material for filtering applications is evaluated.

2 Experimental procedure

2. 1 Fabrication

SiC-based biomorphic ceramics were fabricated by reactive infiltration of carbon preforms with molten silicon, following a procedure extensively reported elsewhere [16, 20-23]. For this work, five wood species were used as starting precursors: four natural woods, Ayous (*Triplochiton scleroxylon*), Pine (*Pinus Sylvestris*), Iroko (*Chlorophora excelsa*), Red oak (*Quercus rubra*), and one processed wood, a medium-density fiberboard (MDF) made by the hot-pressing of recycled wood fibers. These five different wood precursors were selected to encompass a wide range of microstructures.

The wood samples were first dried (70°C, 24 h) and pyrolyzed in an inert atmosphere using a slow heating rate of 0.5°C min^{-1} up to 500°C to avoid crack formation. Afterwards, a higher heating rate of 1°C min^{-1} up to a peak temperature of 900°C was used, followed by a soak time of 30 min. Pyrolyzed preforms of carbon were machined to near-net shape into disks 25.4 mm in diameter and 3 mm in thickness from sections cut perpendicular (*axial samples*) and parallel (*radial samples*) to the tree-growth direction. Therefore, the axial direction is parallel to the tree-growth axis, and the radial direction is perpendicular to it. Carbon preform sections from MDF wood cut perpendicular to the direction of compaction were considered as radial samples.

Then, pyrolyzed preforms of carbon were infiltrated in vacuum with molten silicon (Silgrain HQ-99.7% purity; Eljem Silicon, Oslo, Norway) at 1550°C for 30 min with a Si:C weight ratio of 3.5. This ratio is higher than the stoichiometric ratio, but was necessary to ensure the complete reaction of the carbon preforms. After infiltration, the final material was a Si/SiC composite with porosity partially filled with residual Si. No geometrical volume changes were detected after the infiltration step. The unconsumed Si was removed by capillary extraction and evaporation at high temperature to produce a porous material. In this process, ceramic specimens placed on top of porous carbon preforms were heat treated up to 1800°C in vacuum at a heating rate of 8°C min^{-1} followed by a soaking time of 4 h. Throughout the text, samples produced by this procedure will be referred to as bioSiC samples.

2.2 Microstructural characterization

The bulk (geometrical) density of the samples was determined by measuring the weight and volume of the cylindrical specimens. The volume fraction of porosity was calculated from the ratio of the measured bulk density to the theoretical density of the fully dense silicon carbide (Porosity (%) = $1-\rho_{bulk}/\rho_{theoretical}$). The theoretical density of the fully dense SiC was considered to be 3.21 g/cm^3 [30]. The specific surface area was measured by krypton adsorption at 77K according to the BET method (ASAP 2420, Micromeritics, Norcross, GA, USA). A scanning electronic microscope (SEM, Jeol 6460-LV) was used to characterize and analyze the microstructure of the resulting porous bioSiC ceramic materials. Mercury intrusion porosimetry was performed to determine the pore-size distribution and average pore diameter

(Pore Master 60 GT, Quantachrome Instruments Inc., Florida, USA). One sample of each wood-based bioSiC was tested. The most relevant microstructural parameters are summarized in Table 1. Errors from bulk density and volume fraction of porosity represent one standard deviation from 36 samples fabricated for each precursor.

2. 3 Permeability measurements

The pressure drop of a gas flowing through a porous material is described as follows by Forchheimer's equation [31], determined by Darcy's law and Forchheimer's extension:

$$\frac{\Delta p}{L} = \frac{\eta}{k_1} v + \frac{\rho}{k_2} v^2 \quad (1)$$

where Δp is the pressure drop (Pa), L is the thickness of the sample (m), η is the dynamic viscosity (Pa·s), v is the gas velocity ($m \cdot s^{-1}$), ρ the gas density ($kg \cdot m^{-3}$) and k_1 and k_2 are the Darcian (m^2) and inertial (m) permeabilities, respectively. In the case of compressible fluids, the pressure is determined by the difference in the squares of input (P_i) and output (P_0) pressure, and is determined as follows:

$$\Delta P = \frac{P_i^2 - P_0^2}{2P_0^2} \quad (2)$$

A laboratory-made gas permeameter device was designed and built to study the permeability of the bioSiC specimens. This experimental apparatus has been described elsewhere [24, 32] and a diagram of this device is shown in Figure 1. In this apparatus, bioSiC samples of 25.4 mm in diameter and 3 mm in thickness from the five different precursors were inserted in sealed clamps, and a gas flow was forced to cross the porous samples while the pressure and gas flow input and output were being measured. Gas flow through the sample was measured by a rotameter depending on the pressure drop measured by a gas manometer from 1 to 9 kPa. Compressed air was used as the working medium at room temperature while the dynamic viscosity, taking into account the temperature at which samples were tested, was taken from the literature ($\eta = 1.8 \cdot 10^{-5}$ Pa·s, $\rho = 1.17$ kg/m^3) [33]. Calibration experiments which measured a pressure drop in the system without a sample were performed to determine the real pressure drop during sample testing. The gas-flow velocity v was determined by the measured volumetric flow rate Q per unit of cross-sectional area A (m^2) perpendicular to the flow direction ($v = Q/A$).

The experimental curves of pressure drop as a function of flow velocity were fitted according to Forchheimer's equation for compressible fluids. From these quadratic fits, permeability constants, k_1 and k_2, were determined according to Eq. 1. Both parameters were considered constant and independent of the flow conditions because they have been found to depend only on the relevant microstructural parameters, such as morphology, pore-size distribution, porosity fraction or connectivity [26]. Darcy's law considers only the pressure drop associated with laminar viscous effects at very low flow velocities,

reflecting a linear behavior between the pressure drop and the air-flow velocity in a porous medium. However, also considering Forchheimer's extension for higher velocities, the pressure gradient shows a more realistic parabolic trend due to turbulence and inertial effects [34]. The reported permeability values are the average of the measurement of three samples for each type of wood precursor and orientation. Errors represent one standard deviation.

2. 4 Mechanical characterization

For the study of the mechanical robustness of the samples, compressive-strength tests were performed. Parallelepipeds with dimensions of (3x3x5) mm^3 were cut with a diamond saw and then tested in compression up to failure at a constant strain rate of $2 \cdot 10^{-4}$ s^{-1} at room temperature, using a screw-driven universal testing machine (Microtest EM1/20/FR, Madrid, Spain). The compressive load was applied along the long axis of the samples using alumina rods. The reported maximum compressive strength was the average of a minimum of five measurements for each wood-bioSiC and loading conditions in both directions (axial and radial). Error bars represent one standard deviation.

3. Results and discussion

3. 1 Microstructure

Figure 2 and Figure 3 show SEM micrographs of porous bioSiC samples for sections perpendicular (axial) and parallel (radial) to the growth direction, respectively. After the reactive infiltration process and the Si removal step, the resulting bioSiC samples consisted of SiC scaffolds with highly interconnected porosity aligned with the tree-growth direction, that replicated the strongly anisotropic cell-wall structure of the natural wood precursor [35] (Figure 2). The larger pores were free of silicon, although residual unreacted silicon in some pores of smaller size could not be completely removed due to capillarity effects. The anisotropic character of the resulting material and the interconnection of the long channels parallel to the tree-growth axis described above, is shown in Figure 3 for radial samples.

In the case of bioSiC from wood of MDF, the micrographs were taken in a section perpendicular to the direction of fiber compaction. Due to its microstructure of oriented fibers, the orientation of its pores and similarity with the pore distribution in the case of samples from natural woods, sections perpendicular to the direction of compacting fibers were classified as radial samples. Although it was found that its microstructure also presented an anisotropic character [36], which was determined by the manufacturing and compaction process employed, their properties were studied only in the radial direction.

3. 2 Gas permeability

For the determination of the permeability of bioSiC materials from different wood precursors, three samples for each precursor and orientation (axial and radial) were tested to ensure repeatability. The average experimental pressure drops per unit of length as a function of air-flow velocities for bioSiC samples are plotted in Figure 4 along with the fit to Forchheimer's equation (Eq. 1).

It can be noted that the pressure drop increased with the gas-flow velocity. The experimental data generally showed a good fit to the quadratic dependence with air-flow velocity, with least-squares coefficients $r^2 > 0.998$. Darcian and inertial permeability parameters k_1 and k_2, respectively [31], were calculated from these fits and are shown in Table 2. For all bioSiC samples in the axial direction, except for Pine-bioSiC, k_1 was at the same order of magnitude (10^{-11} m^2) in contrast to radial samples for which all values were around 10^{-12} m^2, an order of magnitude lower. k_2 for all axial samples was in the range of 10^{-7} m, and 10^{-8} m in the case of radial samples.

3. 3 Microstructure Dependence

Relevant microstructural parameters such as pore size, surface area and total porosity were studied thoroughly to understand their influence in the permeability values because, as observed, the permeability values differed up to one order of magnitude due to the difference in microstructure of each precursor and orientation. In previous works on porous ceramics, gas permeability proved to be directly dependent on the total pore-volume fraction [32], tortuosity, and the average pore size of the sample [29, 32, 37, 38]. Figure 5 shows pore-size distributions and Table 1 lists pore sizes from mercury intrusion porosimetry (an explanation to how axial and radial pore sizes were calculated can be found in section 3.4). Samples of bioSiC from wood of Ayous, Red Oak or Iroko showed different ranges of pore size in the interval from 0.1 to 400 μm, showing a multimodal and heterogeneous pore-size distribution, while in the case of bioSiC from Pine and MDF, the pore-size distributions were narrower and more homogeneous.

Orientation dependence were observed for bioSiC for other properties such as thermal conductivity [39, 40] or mechanical strength [24] and, as expected, due to the anisotropic structure itself of the wood precursor (Figure 2 and Figure 3), samples also showed an orientation-dependent permeability (Figure 4 and Table 2). The results depended on the direction of the air flow compared to the direction of the sample because permeability is inversely proportional to tortuosity [41]. In all samples, permeability was higher in the axial direction because for a given air velocity, radial samples showed a greater pressure drop. This trend may be attributed to the orientation of the elongated pores and their interconnectivity compared with the direction of the gas flow causing less tortuosity of the air flow. In permeability tests, gas flow was expected to flow more easily through the larger and interconnected pore channels in axial samples, in contrast to radial samples where the direction of gas flow was perpendicular to the elongated

channels. In the case of Iroko-bioSiC (Figure 3), the sample also had larger interconnected pores perpendicular to the tree-growth direction and thus resulted in greater permeability in this direction compared to the other radial samples, deviating from the observed general trend.

It is important to keep in mind that usually accessible techniques for porosity and surface area determination, such as gas adsorption or mercury intrusion porosimetry, yield scalar, volume averaged values of the pore size distribution even for an anisotropic material. This is so because the gas or Hg will penetrate all interconnected pores irrespectively of their orientation, whereas in a permeability experiment only those aligned with the gas stream will contribute significantly to flow.

3.4. Permeability prediction

As observed, permeability depended strongly on the wood precursor and pore direction selected, so that it would be useful to predict the permeability of a sample previously, attending to its microstructural parameters for assessing its viability in subsequent filtering applications. Some theoretical models in the literature proposed a prediction of permeability in porous media by structural parameters, the most popular among these having been developed by Ergun [42]. This model proposes a general correlation between pressure drop and gas-flow velocity when a fluid flows through granular beds. From this model the permeability constants are given by:

$$k_1 \propto \frac{\varepsilon^3 d_p^2}{(1-\varepsilon)^2} \quad (3)$$

$$k_2 \propto \frac{\varepsilon^3 d_p}{(1-\varepsilon)} \quad (4)$$

where ε is the volume fraction of porosity and d_p is defined as an equivalent particle diameter of the granular media. Based on previous studies of cellular materials, d_p can be replaced by an equivalent pore diameter, d [28, 43]. When the grains of the samples are spherical, the following relationship between particle size and pore size is proposed [1]:

$$d_p = \frac{3}{2}\frac{(1-\varepsilon)}{\varepsilon} d \quad (5)$$

Permeability constants from this modification of Ergun's model, taking into account an equivalent pore size, can be rewritten as:

$$k_1 = \frac{\varepsilon\, d^2}{A} \quad ; \quad k_2 = \frac{\varepsilon^2 d}{B} \quad (6)$$

In previous works, Ergun equations agreed reasonably well with k_1, but these overestimated the inertial term [1, 28]. Since Ergun's model normally did not provide an overall agreement with experimental data because it was developed for granular beds, and this is not suitable for cellular materials, many researchers have considered these equations modifiable and have already proposed different numerical

constants and empirical parameters related to the microstructure of each cellular material [26, 43]. A review on this subject has been presented by Macdonald et al. [44]. Most previous works assumed a monomodal and isotropic porosity and their applicability to bioSiC is questionable since it exhibits a complex anisotropic porous microstructure consisting of a SiC scaffold formed by a cluster of SiC grains and a multimodal pore size distribution inherited from the wood precursor, so that it is more difficult to model the gas flow forced to travel through these porous media instead of isotropic materials [45, 46]. In particular, for a bimodal pore size distribution such as that observed in bioSiC for the axial direction, there is a difficulty in selecting the equivalent pore size *d* since the arithmetic mean will be biased towards the most abundant but smaller narrow channels thus underestimating the effective pore size. Fortunately, the effective pore size can be calculated from the pore size distribution accessible through Hg intrusion porosimetry.

Let us consider a set of cylindrical channels of radius r_i and length L, then the flow through them for a given pressure drop ΔP can be calculated using the Hagen-Poiseuille relationship:

$$Q_i = \frac{\Delta P}{8\eta L}\,\pi r_i^4 = \frac{\Delta P}{8\eta L}\,\pi r_i^2 \cdot r_i^2 \tag{7}$$

Dividing by the total area we find the flow per unit area:

$$q_i = \frac{\Delta P}{8\eta L}\frac{\pi r_i^2}{A} r_i^2 = \frac{\Delta P}{8\eta L}\alpha(r_i) \cdot r_i^2 \tag{8}$$

Where $\alpha(r_i)$ represents the area fraction of the pores with radius r_i. If the pores are perfect, aligned cylinders then $\alpha(r_i)$ is equal to $f(r_i)$, the volume fraction of pores of radius r_i, a quantity directly measured by porosimetry. Summing the contribution of all types of and using $v = \epsilon q$ one finds:

$$v = \varepsilon \frac{\Delta P}{8\eta L} \sum_i f(r_i) r_i^2 \tag{9}$$

And thus the linear permeability is, in terms of the pore diameter $d_i = 2r_i$:

$$k_1 = C\varepsilon\overline{d^2} \tag{10}$$

Where *C* is a constant that describes the pore geometry and is equal to 1/32 for cylindrical pores and:

$$\overline{d^2} = \sum_i f(r_i) r_i^2, \qquad \sum_i f(r_i) = 1 \tag{11}$$

Thus, according to this calculation, the relevant pore size is not the mean but instead the square root of the quadratic mean, which is biased towards the larger pores. This is reasonable since flow depends on the fourth power of the pore radius and thus pores twice as large will carry 16 times the flow for a given pressure drop.

Due to the anisotropy of bioSiC, we should use two equivalent pore sizes, one for the axial and another for the radial direction, if we want to rationalize the measured permeabilities in terms of the microstructure. Unfortunately the measured pore size distribution is an orientation-average of the anisotropic one, and thus we need to find a criteria for the calculation of effective pore sizes. Since bioSiC exhibits large channels only in the axial direction, and these are in general larger than 100 μm, we propose that for the axial direction we should use Eq. 11 using the whole pore size distribution, including the contribution of the larger pores. Since however there are no large channels in the radial direction, we propose to use the same approach but now with a cutoff in the pore size distribution of 100 μm. Up to that pore size, the distribution is mostly monomodal and thus the effective pore size is very close to the mean pore size.

Since the porosities of all the materials studied here are similar (except for the *Ayous*-derived material), we can plot k_1 vs d to find a trend with pore size. To this end Figure 6. A) shows measured permeability vs. effective pore size, calculated using the criteria described above.

As has been shown, permeabilities can also be described in terms of the surface area per unit volume S_v as [47]:

$$k_1 = \frac{\varepsilon^3}{\alpha\, S_v^2 (1-\varepsilon)^2} \quad ; \quad k_2 = \frac{\varepsilon^3}{\beta\, S_v (1-\varepsilon)} \tag{12}$$

where α and β are parameters that depend on the microstructure and are fitted to each porous material [44]. The geometrical surface area in Eq. 12 may be determined either experimentally or by assuming a model that describes the real geometry of the pores. Richardson et al. [47] examined three models [48] for estimating S_v in ceramic foams and found values that were similar to each other and proposed empirical equations for α and β in terms of the average pore size and porosity, providing a good prediction of permeability constants. In particular, if porosity is described as a set of parallel cylinders with a constant diameter based on the hydraulic diameter model developed by Kozeny, the geometrical surface area may be determined as follows [47]:

$$S_v = \frac{4\varepsilon}{d\,(1-\varepsilon)} \tag{13}$$

And substituting Eq. (13) in Eq. (12) the Ergun model is recovered. The main problem with applying the model of Eq. (13) lies in the choice of a relationship between pore size and surface area per unit volume, and again the use of a single parameter for a material with an anisotropic, multimodal pore size distribution is questionable. The surface area can be estimated from the pore size distribution again considering that, for cylindrical pores:

$$S = 2\int_0^{V_p} \frac{dV}{r} = 2V_p \int_0^1 \frac{dV}{r} \tag{14}$$

Which is deduced from the area to volume ratio of a cylinder; V_p is the volume of pores. Dividing by the total volume and writing the equation in discrete form:

$$S_v = 2\varepsilon \sum_i \frac{f(r_i)}{r_i} = 4\varepsilon \sum_i \frac{f(d_i)}{d_i} \quad (15)$$

Thus we could use Eq. (15) in conjunction with the Kozeny-Carman relationship of Eq. (12) to estimate an equivalent pore size. The validity of Eq. (15) for bioSiC can be tested by plotting the values of S_v measured directly from Kr adsorption against those calculated from pore size distribution data. Figure 6. B) shows that this correlation is reasonable. However, calculations of equivalent pore sizes from this approach yielded values in the 5 – 7 μm which are clearly too low to adequately represent the microstructural average in these materials. In the same way as the quadratic mean estimate results in effective pore sizes larger than the mean because it is weighted towards the larger channels, effective pore sizes calculated from surface areas are biased towards the smaller channels, which contribute the most to the surface area.

Panels A and B of Figure 7 plots measured viscous and inertial permeabilities against εd^2 and $\varepsilon^2 d$, respectively, as predicted by the Ergun relations of Eq. (6), where the values of d were chosen as different averages of the pore size distribution depending on whether the axial or radial orientations were considered, according to the previous discussion. For the viscous permeability, a reasonable agreement was found when $A = (80 \pm 1)$ μm², whereas the inertial permeability did not follow Ergun's relationship. Instead, it was essentially constant for a given orientation, yielding $(11.8 \pm 0.8) \cdot 10^{-8}$ m and $(5 \pm 3) \cdot 10^{-8}$ m for axial and radial orientations, respectively.

These correlations can help to predict the range of permeability of porous SiC ceramics, although several precautions must be kept in mind. First, bioSiC samples do not have a set of perfectly cylindrical pores and thus deviations may occur. In addition, it is worth bearing in mind that not all the porosity may be available for fluid flow and the average pore size considered on the permeability constants from these models were calculated by intrusion porosimetry, which was a gross simplification because the whole size distribution of bioSiC samples was reduced to a single mean value [41, 43], making it perhaps the greatest source of error. These models would also be improved by including additional microstructural parameters for complex structures such as tortuosity of the porous media which reflect the anisotropy of this material in both directions. Nevertheless, the predicted values from the proposed agreed reasonably with those calculated experimentally at least for the linear permeability and thus could be useful as a first benchmark to determine whether a wood precursor would be valid for a particular application.

3.4 Flow regime

The Reynolds number R_e for porous media is defined as the ratio between inertial and viscous effects, and allows the linear and nonlinear flow behavior to be predicted [41]. R_e is defined as:

$$R_e = \frac{\rho\, v_i d}{\eta} \tag{16}$$

where v_i is the interstitial fluid velocity, which can be calculated between the difference on superficial velocity and the porosity ($v_i = v_s \cdot \varepsilon^{-1}$). For a Reynolds number less than one ($R_e < 1$), the energy is dissipated due to viscous friction and the pressure drop can be determined simply by applying Darcy's law. For Reynolds numbers ranging between $1<R_e<150$, the flow is also predominantly laminar but inertial effects at a small proportion are already present in the flow, while for R_e >150-300 the flow is mainly turbulent and unsteady.

Due to the difficulty of determining a representative pore size in complex porous media, Ruth and Ma proposed an alternative model in order to assess the flow regime [49], where relative contributions of viscous and inertial effects on total pressure drop when a gas is flowing through a porous medium could be determined by the dimensionless Forchheimer's number [28]. It was defined as a function of the permeability constants according to Eq. 17.

$$F_0 = \frac{\rho v}{\eta} \frac{k_1}{k_2} \tag{17}$$

For $F_0<<1$, viscous effects are dominant on the flow, while for $F_0>>1$ the pressure drop is due mainly to inertial effects [50]. The individual contributions of viscous and inertial effects to total pressure drop from this parameter can thus be estimated as follows:

$$\frac{\Delta P_{viscous}}{\Delta P_{total}}(\%) = \frac{1}{1+F_0} \tag{18}$$

$$\frac{\Delta P_{inertial}}{\Delta P_{total}}(\%) = \frac{F_0}{1+F_0} \tag{19}$$

Table 3 reports the calculated F_0 and Figure 8 shows the dependence of both viscous and inertial contributions to the total pressure drop of each wood-bioSiC as a function of sample orientation under air-flow velocities ranging from 0.01 to 0.4 $m \cdot s^{-1}$. It was noted that the flow regime depended heavily on the direction of the sample. At very low gas velocities (0.01 $m \cdot s^{-1}$), the pressure drop in both orientations was due mainly to viscosity effects. Nevertheless, as air velocity increased, the contribution of inertial effects to total pressure drop became more remarkable in axial samples, being close to 90% at the highest velocity. Conversely, in radial samples viscosity effects were more efficient, showing a gentler drop with increasing flow velocity. At the highest velocity the ratio of the inertial part to the whole flow was close to 50%. This trend was also observed in the experimental curves shown in Figure 4. The pressure drop

for radial samples was more consistent with Darcy's law, following a linear trend with the increase in velocity, implying that flow was mainly laminar and losses of viscous energy were due to friction between gas layers [31].

Differences in the two contributions depending on the direction were due mainly to the anisotropy and the tortuosity of bioSiC, as well as the presence of large axial channels. In axial samples, air flow traversed the straight, mostly cylindrical axial channels running to the sides of the samples with lower tortuosity than in the case of radial samples where, due to the absence of interconnected channels, the air flow travelled through the sample from the SiC grain boundaries, resulting in an orderly and laminar flow. For a given flow rate, inertial effects and turbulent flow will be more significant in the axial direction as the effective pore size and thus Reynolds number is higher than in the radial direction.

3.5 Mechanical stability

In Figure 9-A a comparison of maximum compressive strengths as a function of density is provided for each wood-derived SiC specimen for the two different orientations. The average of the maximum strength were determined from a minimum of five measurements for each precursor. Although stress-strain curves are not shown, the fracture of the samples was catastrophic and brittle without plastic deformation. As can be seen from Table 4 and Figure 9-A, compressive strength was in the range ~3-115 MPa, showing a dependence on density and orientation of the wood precursor. In both directions, the values approximated a potential relationship with the relative density. The values decreased significantly with decreasing density of the samples, in direct relation to the porosity fraction. This result agrees with findings in previous works [22, 23, 51], in which the mechanical strength of these ceramic samples depended on density. Consequently, greater pore volume gradually diminished the mechanical strength.

The anisotropic character also affected the compressive strength. Maximum compressive strength proved higher when the load was applied parallel to the growth direction (axial) ranging from 8 to 88 MPa, resulting in a greater mechanical stability. In contrast, when measurements were in the radial orientation maximum compressive strengths were 1.4-3.2 times lower (Table 4), ranging from 2 to 10 MPa in bioSiC derived from natural wood. Although samples from MDF-wood were considered radial samples due to their microstructure, their compressive strength differ greatly from natural wood-derived bioSiC because of the difference in microstructure and because of a more homogeneous pore size distribution. The values were higher than expected in relation to their density because some fibers could be oriented in the direction of maximum compressive load, which yielded a higher compressive strength [24].

In Figure 9-B the relative strength data ($\sigma_{bioSiC}/\sigma_{SiC}$) is plotted as a function of the relative density that determines the SiC volume fraction (ρ_{bioSiC}/ρ_{SiC}). These factors may be related to a potential dependence according to the following equation given by the model of Gibson and Ashby [48]:

$$\frac{\sigma_{bioSiC}}{\sigma_{SiC}} = \left(\frac{\rho_{bioSiC}}{\rho_{SiC}}\right)^{n} \quad (20)$$

Where σ_{bioSiC} and ρ_{bioSiC} are the strength and the bulk density of the porous solid (bioSiC), σ_{SiC} and ρ_{SiC} are the strength and the density of a fully dense SiC monolith, and n is a geometric exponent which depends on the microstructure and loading direction. Values of compressive strength (3.9 GPa) and theoretical density of fully dense SiC (3.21 g cm^{-3}) were taken from the literature [30, 52]. Since the exponent *n* is derived from the fitting of log-log plots, its calculation does not depend on the actual numerical values assigned to the bulk properties of the solid phase. Due to the porosity of the material, the values found here were much lower than the strength for the fully dense material. The exponent was higher than predicted by the model (3.78 for axial samples and 3.19 for radial samples), but consistent with previous works confirming that this model results in an overestimation when applied to porous bioSiC samples derived from wood [23, 52]. Since MDF samples performed more like axial samples than radial samples, the geometric exponent *n* was determined by fitting the values of radial samples without considering the results of MDF.

The compressive strengths of bioSiC specimens measured in this work were slightly lower or comparable to other values reported in the literature in relation to their densities [22, 23]. Lower values could be due to two factors. BioSiC specimens could contain a small proportion of unreacted carbon after molten silicon infiltration, which has been demonstrated to weaken mechanical properties [53]. Additional differences could be due to the use of capillary extraction and evaporation instead of chemical etching used in other works [22, 24].

3.6 Applicability as a filter material

Filter materials are selected according to pore structure and microstructural parameters [54]. Small pore sizes and low volume fractions of porosity enhance filtration efficiency and the mechanical stability of the samples, while at the same time the pressure drop in the filter increases with the gas flow. Consequently, a tradeoff needs to be found between mechanical robustness and pressure drop.

Pore volume in most commercial filters is within the range of 40-50% or exceptionally 60% [13]. Furthermore, typically a well-defined monomodal pore distribution is sought for improved particle-filtration efficiency and filter selectivity [13, 55]. Therefore, ceramic filter substrates normally present pore volumes of about 50% and average pore sizes of 10μm. Regarding the five precursors used in this work, the level of porosity was controlled by selecting a wood precursor. Ayous, Red Oak and Iroko

showed a multimodal pore-size distribution with larger pores up to hundreds of micrometers. In this way, Pine and MDF had more desirable characteristics, because of their narrower and more homogeneous pore distributions.

From the knowledge of the influence of microstructure on permeability values, it is possible to estimate the pressure drop originated in a filter under a given flow rate. Innocentini et al. [56] have classified a wide range of porous materials according to permeability parameters. In Figure 10 we show an adapted version of the map from the studies of Innocentini et al. including all the results found in the present work for bioSiC materials, the results for other filter ceramics of cordierite-bonded porous SiC for comparison purposes [1] and the exponential fit that relates permeability parameters of a variety of porous media [(k_2=exp(-1.71588·$k_1^{-0.08093}$)]. Permeability of porous bioSiC materials were located according to the classification in the typical range for granular and fibrous filters, which normally present Darcian permeabilities in the range 10^{-9}–10^{-13} m^2. For axial samples, permeability values deviated slightly from the general trend (Figure 10) and were generally higher than other values reported in the literature for commercial granular filters because of the presence of interconnected larger pores with preferred orientation.

Alonso-Fariñas et al. [25] and Bautista et al. [24] assessed the feasibility of porous MDF-derived bioSiC as high-temperature filters in gasification plants with permeability values of 10^{-13} m^2 for porosities ranging from 40-60%, and with a filtration efficiency higher than 98%. In ceramic materials used as diesel particulate filters, permeability typically ranges from 10^{-12} to 10^{-9} [13]. Eom et al. [37] reported permeability values of macroporous SiC ceramics on the order of 10^{-12}-10^{-13} m^2 with porosities of 50-60%. For a volume of porosity of 75%, Song et al. [57] reported permeability values in the range of $10^{-13}m^2$ and Yan et al. [38] reported values in the range of 10^{-12} m^2 on porous cordierite-mullite ceramic samples with porosity of 40-50%. According to the map in Figure 10, and permeability values of commercial filters, bioSiC seems to be a promising material for filtering applications.

In terms of mechanical stability, all samples have enough strength not to fail during filtration applications despite their high porosities. Nevertheless, Ayous-bioSiC showed notably poor mechanical stability as a consequence of the high porosity-volume fraction and may not be a suitable precursor for filter applications.

4 Conclusions

Porous biomorphic silicon carbide samples were fabricated from five wood precursors in order to study their feasibility as filter materials. Samples with porosity fractions (45-72%) and a diversity of microstructures resulted. Dependence of permeability and mechanical strength on microstructural parameters was evaluated.

Gas permeability was investigated in air-flow experiments with the control of gas flow and pressure drop. Forchheimer's equation for compressible fluids was applied to the experimental data to determine permeability constants. Experimental room temperature k_1 and k_2 permeabilities were in the range of 10^{-12} to 10^{-13} m^2 and 10^{-7} to 10^{-8} m, respectively, which for application purposes are classified within the range of granular filters and are comparable with permeability values reported by other authors. Average pore size, alignment of pores and tortuosity seemed to be the key factors in permeability results.

For permeability prediction concerning microstructural parameters, we propose an Ergun-type relationship where the equivalent pore size is determined by integration of the pore size distribution, although to different integration limits in the axial and radial directions to reflect the materials' anisotropy. The flow performance of the material was characterized by calculating the Forchheimer's number. We showed that in radial samples inertial effects were not as remarkable as in axial samples, but both terms of Forchheimer's equation must be considered for flow-regime prediction. On the other hand, compressive strength has been found to diminish with porosity, the resulting values being from 3 to 115 MPa.

All the results pointed to the possibility of tailoring these two properties by selecting a particular wood precursor and controlling the microstructural parameters of the final porous ceramics. With the control of these properties, the best optimum requirements for filtering applications of the end product may be fulfilled. Among the precursors studied, the four porous bioSiC materials derived from natural woods showed important orientation-dependent properties. In that way, MDF-bioSiC may be the best candidate, because it presented promising properties: interconnected uniform porosity (49%), narrower and uniform pore-size distribution (3-30μm), reproducible homogeneous microstructure that can be more easily machined into complex shapes compared to natural woods, permeability in an appropriate range and adequate structural strength (115 MPa) despite its high porosity.

Acknowledgements

The Spanish Ministry of Economy and Competitiveness (MINECO) funded this work under grant MAT2013-41233-R. M. P Orihuela is grateful to the MINECO for a predoctoral grant. Electron microscopy, mercury-intrusion porosimetry and specific surface-area measurements were performed at the CITIUS central services of the University of Seville (Spain).

Captions

Figure 1. Schematic diagram of the laboratory-made gas permeameter device for the determination of experimental permeability.

Figure 2. Secondary electrons SEM micrographs of porous bioSiC from the four natural wood precursors used (axial samples). Scale bar is 200 μm.

Figure 3. Secondary electrons SEM micrographs of porous bioSiC from the five wood precursors used (radial samples). Scale bar is 200 μm.

Figure 4. Pressure drop per unit of length as a function of air-flow velocity for the five wood-derived SiC in both axial and radial orientations. Solid symbols correspond to the measurements in axial samples while hollow symbols correspond to radial samples. The solid lines represent the parabolic fitting ($y=ax+bx^2$) according to Forchheimer's equation.

Figure 5. Pore-size distributions of bioSiC specimens from different wood precursors.

Figure 6. A) Permeability vs. effective pore size for bioSiC samples from different precursors, in two orientations. B) Specific surface area per unit volume calculated from the pore size distribution vs. S_v measured from Kr adsorption. See text for details.

Figure 7. A) Permeability k_1 vs. εd^2 and B) inertial permeability k_2 vs. $\varepsilon^2 d$ as dictated by Ergun's relationships, in both axial and radial directions.

Figure 8. Viscous and inertial terms as a percentage of total pressure drop, as a function of air-flow velocity in both directions (axial and radial). Lines are included as a guide to the eye.

Figure 9. A) Maximum compressive strength at room temperature as a function of density for both orientations (error bars equal one standard deviation) and B) Relative strength as a function of relative density from porous SiC-derived ceramic. Solid symbols correspond to axial samples while blank symbols correspond to radial samples. The slope value, which corresponds to the value of n, was 3.7 for axial samples while for radial samples it was 3.19.

Figure 10. Classification of filter materials according to permeability values from the literature. Experimental data from this work was included for comparison purposes. Solid symbols correspond to the measurements in axial samples while hollow symbols correspond to radial measurements.

Tables

Table 1. Relevant microstructural parameters of bioSiC ceramics from the five different wood precursors used in this work.

Precursor	Density (g/cm^3) Wood	Density (g/cm^3) Porous bioSiC	Porosity (%)	Specific Surface (m^2/g)	Radial pore size (μm)	Axial pore size (μm)
Ayous	0.30 ± 0.01	0.88 ± 0.07	72 ± 2	0.13 ± 0.01	19.2	52
Pine	0.48 ± 0.02	1.40 ± 0.08	57 ± 2	0.07 ± 0.01	18.3	32
Iroko	0.60 ± 0.02	1.65 ± 0.11	48 ± 3	0.04 ± 0.01	18.7	58
Red Oak	0.66 ± 0.03	1.76 ± 0.13	45 ± 4	0.05 ± 0.01	18.2	47
MDF	0.80 ± 0.01	1.64 ± 0.11	49 ± 4	0.07 ± 0.01	15.7	

Table 2. Permeability constants determined for both orientations, axial and radial. (Errors represent one standard deviation from the measure of three samples for each wood precursor and orientation)

Orientation	Precursor	Darcian Permeability k_1 (10^{-12} m^2)	Inertial Permeability k_2 (10^{-8} m)
Axial	Ayous	36 ± 9	13.0 ± 1.2
	Pine	9.4 ± 1.5	11.4 ± 0.7
	Iroko	46 ± 17	11.6 ± 0.2
	Red Oak	12 ± 2	11.2 ± 0.7
Radial	Ayous	2.2 ± 0.5	6.7 ± 1.6
	Pine	1.8 ± 0.1	5.7 ± 0.1
	Iroko	5.4 ± 1.2	10 ± 2
	Red Oak	1.1 ± 0.2	2.2 ± 0.7
	MDF	1.0 ± 0.1	2.1 ± 0.8

Table 3. Forchheimer number (F_0) range in both orientations for air-flow velocity ranging from 0.01 to 0.4 m·s^{-1}.

Orientation		Ayous	Pine	Iroko	Red Oak	MDF
Axial	F_0	0.17 - 6.91	0.05 – 2.05	0.25 – 9.89	0.07 – 2.72	-------
Radial	F_0	0.02 - 0.82	0.02 – 0.79	0.03 – 1.35	0.03 – 1.25	0.03 – 1.19

Table 4. Maximum compressive strength of bioSiC.

Precursor	Maximum compressive strength (MPa) Axial	Maximum compressive strength (MPa) Radial	$\frac{\sigma max\ axial}{\sigma max\ radial}$
Ayous	8 ± 3	3 ± 1	2.7
Pine	25 ± 16	12 ± 3	2.1
Iroko	22 ± 5	16 ± 2	1.4
Red Oak	84 ± 17	26 ± 4	3.2
MDF	-------	115 ± 17	-------

References

[1] Dey A, Kayal N, Chakrabarti O, Caldato RF, André CM, Innocentini MDM. Permeability and Nanoparticle Filtration Assessment of Cordierite-Bonded Porous SiC Ceramics. Industrial & Engineering Chemistry Research. 2013;52:18362-72.
[2] Carvalho AC, Raupp-Pereira F, Rodrigues Neto JB, Novaes de Oliveira AP. A new source for production of ceramic filters. Materials Letters. 2015;145:250-2.
[3] Danwittayakul S, Dutta J. Controlled growth of zinc oxide microrods by hydrothermal process on porous ceramic supports for catalytic application. Journal of Alloys and Compounds. 2014;586:169-75.
[4] Villanueva HHS, de Mello PEB. Heat transfer and pressure drop correlations for finned plate ceramic heat exchangers. Energy. 2015;88:118-25.
[5] Fukushima M, Yoshizawa Y-i. Fabrication and morphology control of highly porous mullite thermal insulators prepared by gelation freezing route. Journal of the European Ceramic Society. 2016;36:2947-53.
[6] Yakimova R, R. M. Petoral J, Yazdi GR, Vahlberg C, Spetz AL, Uvdal K. Surface functionalization and biomedical applications based on SiC. Journal of Physics D: Applied Physics. 2007;40:6435.
[7] Das I, De G, Hupa L, Vallittu PK. Porous SiO2 nanofiber grafted novel bioactive glass–ceramic coating: A structural scaffold for uniform apatite precipitation and oriented cell proliferation on inert implant. Materials Science and Engineering: C. 2016;62:206-14.
[8] Matti Maricq M. Chemical characterization of particulate emissions from diesel engines: A review. Journal of Aerosol Science. 2007;38:1079-118.
[9] McClellan RO, Hesterberg TW, Wall JC. Evaluation of carcinogenic hazard of diesel engine exhaust needs to consider revolutionary changes in diesel technology. Regulatory Toxicology and Pharmacology. 2012;63:225-58.
[10] Prasad R, Bella VR. A Review on Diesel Soot Emission, its Effect and Control. Bulletin of Chemical Reaction Engineering & Catalysis; 2010: BCREC Volume 5 Issue 2 Year 2010. 2011.
[11] Fiebig M, Wiartalla A, Holderbaum B, Kiesow S. Particulate emissions from diesel engines: correlation between engine technology and emissions. Journal of Occupational Medicine and Toxicology. 2014;9:6.
[12] Guan B, Zhan R, Lin H, Huang Z. Review of the state-of-the-art of exhaust particulate filter technology in internal combustion engines. Journal of Environmental Management. 2015;154:225-58.
[13] Adler J. Ceramic Diesel Particulate Filters. International Journal of Applied Ceramic Technology. 2005;2:429-39.
[14] Yang J, Stewart M, Maupin G, Herling D, Zelenyuk A. Single wall diesel particulate filter (DPF) filtration efficiency studies using laboratory generated particles. Chemical Engineering Science. 2009;64:1625-34.
[15] Roewer G, Herzog U, Trommer K, Müller E, Frühauf S. Silicon Carbide — A Survey of Synthetic Approaches, Properties and Applications. High Performance Non-Oxide Ceramics I: Springer Berlin Heidelberg; 2002. p. 59-135.
[16] de Arellano-López AR, Martínez-Fernández J, González P, Domínguez C, Fernández-Quero V, Singh M. Biomorphic SiC: A new engineering ceramic material. International Journal of Applied Ceramic Technology. 2004;1:56-67.
[17] Greil P, Lifka T, Kaindl A. Biomorphic Cellular Silicon Carbide Ceramics from Wood: I. Processing and Microstructure. Journal of the European Ceramic Society. 1998;18:1961-73.
[18] Singh M, Martínez-Fernández J, de Arellano-López AR. Environmentally conscious ceramics (ecoceramics) from natural wood precursors. Current Opinion in Solid State and Materials Science. 2003;7:247-54.
[19] Sieber H, Hoffmann C, Kaindl A, Greil P. Biomorphic Cellular Ceramics. Advanced Engineering Materials. 2000;2:105-9.
[20] Bautista MA, de Arellano-López AR, Martínez-Fernández J, Bravo-León A, López-Cepero JM. Optimization of the fabrication process for medium density fiberboard (MDF)-based biomimetic SiC. International Journal of Refractory Metals and Hard Materials. 2009;27:431-7.
[21] Varela-Feria F, Ramírez-Rico J, de Arellano-López A, Martínez-Fernández J, Singh M. Reaction–formation mechanisms and microstructure evolution of biomorphic SiC. J Mater Sci. 2008;43:933-41.
[22] Torres-Raya C, Hernandez-Maldonado D, Ramirez-Rico J, Garcia-Gañan C, de Arellano-Lopez AR, Martinez-Fernandez J. Fabrication, chemical etching, and compressive strength of porous biomimetic SiC for medical implants. Journal of Materials Research. 2008;23:3247-54.
[23] Kaul VS, Faber KT, Sepúlveda R, de Arellano López AR, Martínez-Fernández J. Precursor selection and its role in the mechanical properties of porous SiC derived from wood. Materials Science and Engineering: A. 2006;428:225-32.
[24] Bautista MA, Cancapa JQ, Fernandez JM, Rodriguez MA, Singh M. Microstructural and mechanical evaluation of porous biomorphic silicon carbide for high temperature filtering applications. Journal of the European Ceramic Society. 2011;31:1325-32.

[25] Alonso-Farinas B, Lupion M, Rodriguez-Galan M, Martinez-Fernandez J. New candle prototype for hot gas filtration industrial applications. Fuel. 2013;114:120-7.
[26] Moreira EA, Innocentini MDM, Coury JR. Permeability of ceramic foams to compressible and incompressible flow. Journal of the European Ceramic Society. 2004;24:3209-18.
[27] Topateş G, Petasch U, Adler J, Kara F, Mandal H. Production and permeability of porous Si3N4 ceramics produced by starch addition. Journal of Asian Ceramic Societies. 2013;1:257-61.
[28] Topates G, Mammitzsch L, Petasch U, Adler J, Kara F, Mandal H. Microstructure–permeability relation of porous β-Si3N4 ceramics. Journal of the European Ceramic Society. 2013;33:1545-51.
[29] Kumar A, Mohanta K, Kumar D, Parkash O. Low cost porous alumina with tailored gas permeability and mechanical properties prepared using rice husk and sucrose for filter applications. Microporous and Mesoporous Materials. 2015;213:48-58.
[30] Snead LL, Nozawa T, Katoh Y, Byun T-S, Kondo S, Petti DA. Handbook of SiC properties for fuel performance modeling. Journal of Nuclear Materials. 2007;371:329-77.
[31] Najmi H, El-Tabach E, Chetehouna K, Gascoin N, Falempin F. Effect of flow configuration on Darcian and Forchheimer permeabilities determination in a porous composite tube. International Journal of Hydrogen Energy. 2016;41:316-23.
[32] Wang B, Zhang H, Phuong H-T, Jin F, Yang J-F, Ishizaki K. Gas permeability and adsorbability of the glass-bonded porous silicon carbide ceramics with controlled pore size. Ceramics International. 2015;41:2279-85.
[33] Kadoya K, Matsunaga N, Nagashima A. Viscosity and Thermal Conductivity of Dry Air in the Gaseous Phase. Journal of Physical and Chemical Reference Data. 1985;14:947-70.
[34] Innocentini MDM, Salvini VR, Pandolfelli VC, Coury JR. Assessment of Forchheimer's Equation to Predict the Permeability of Ceramic Foams. Journal of the American Ceramic Society. 1999;82:1945-8.
[35] Greil P. Biomorphous ceramics from lignocellulosics. Journal of the European Ceramic Society. 2001;21:105-18.
[36] Orlova TS, Popov VV, Quispe Cancapa J, Hernández Maldonado D, Enrique Magarino E, Varela Feria FM, et al. Electrical properties of biomorphic SiC ceramics and SiC/Si composites fabricated from medium density fiberboard. Journal of the European Ceramic Society. 2011;31:1317-23.
[37] Eom J-H, Kim Y-W, Song I-H. Effects of the initial α-SiC content on the microstructure, mechanical properties, and permeability of macroporous silicon carbide ceramics. Journal of the European Ceramic Society. 2012;32:1283-90.
[38] Yan W, Li N, Li Y, Tong J, Luo H. Strength and gas permeability of porous cordierite-mullite ceramics with different phase compositions and microstructures prepared by a pore-forming in-situ technique. Journal of Ceramic Processing Research. 2013;14:109-13.
[39] Parfen'eva LS, Orlova TS, Smirnov BI, Smirnov IA, Misiorek H, Mucha J, et al. Anisotropy of the thermal conductivity and electrical resistivity of the SiC/Si biomorphic composite based on a white-eucalyptus biocarbon template. Phys Solid State. 2006;48:2281-8.
[40] Pappacena KE, Faber KT, Wang H, Porter WD. Thermal Conductivity of Porous Silicon Carbide Derived from Wood Precursors. Journal of the American Ceramic Society. 2007;90:2855-62.
[41] Innocentini MDM, Faleiros RK, Pisani R, Thijs I, Luyten J, Mullens S. Permeability of porous gelcast scaffolds for bone tissue engineering. Journal of Porous Materials. 2009;17:615-27.
[42] Ergun S, Orning AA. Fluid Flow through Randomly Packed Columns and Fluidized Beds. Industrial & Engineering Chemistry. 1949;41:1179-84.
[43] Biasetto L, Colombo P, Innocentini MDM, Mullens S. Gas Permeability of Microcellular Ceramic Foams. Industrial & Engineering Chemistry Research. 2007;46:3366-72.
[44] Macdonald IF, El-Sayed MS, Mow K, Dullien FAL. Flow through Porous Media-the Ergun Equation Revisited. Industrial & Engineering Chemistry Fundamentals. 1979;18:199-208.
[45] Dey A, Kayal N, Chakrabarti O, Caldato RF, Innocentini MDdM, Guerra VG. Investigations on Material and Mechanical Properties, Air-Permeation Behavior and Filtration Performance of Mullite-Bonded Porous SiC Ceramics. International Journal of Applied Ceramic Technology. 2014;11:804-16.
[46] Isobe T, Kameshima Y, Nakajima A, Okada K, Hotta Y. Gas permeability and mechanical properties of porous alumina ceramics with unidirectionally aligned pores. Journal of the European Ceramic Society. 2007;27:53-9.
[47] Richardson JT, Peng Y, Remue D. Properties of ceramic foam catalyst supports: pressure drop. Applied Catalysis A: General. 2000;204:19-32.
[48] L.J. Gibson MFA. Celullar Solids-Structure & Properties. In: Press P, editor.: Cambridge; 1998.
[49] Ma H, Ruth DW. The microscopic analysis of high forchheimer number flow in porous media. Transport in Porous Media. 1993;13:139-60.
[50] Innocentini MDM, Lefebvre LP, Meloni RV, Baril E. Influence of sample thickness and measurement set-up on the experimental evaluation of permeability of metallic foams. Journal of Porous Materials. 2009;17:491-9.

[51] Presas M, Pastor JY, Llorca J, de Arellano-López AR, Martínez-Fernández J, Sepúlveda RE. Mechanical behavior of biomorphic Si/SiC porous composites. Scripta Materialia. 2005;53:1175-80.
[52] Varela-Feria FM, Martínez-Fernández J, de Arellano-López AR, Singh M. Low density biomorphic silicon carbide: microstructure and mechanical properties. Journal of the European Ceramic Society. 2002;22:2719-25.
[53] Calderon NR, Martinez-Escandell M, Narciso J, Rodríguez-Reinoso F. The role of carbon biotemplate density in mechanical properties of biomorphic SiC. Journal of the European Ceramic Society. 2009;29:465-72.
[54] Tandon P, Heibel A, Whitmore J, Kekre N, Chithapragada K. Measurement and prediction of filtration efficiency evolution of soot loaded diesel particulate filters. Chemical Engineering Science. 2010;65:4751-60.
[55] Kittelson DB. Engines and nanoparticles: a review. Journal of Aerosol Science. 1998;29:575-88.
[56] de Mello Innocentini MD, Sepulveda P, dos Santos Ortega F. Permeability. Cellular Ceramics: Wiley-VCH Verlag GmbH & Co. KGaA; 2006. p. 313-41.
[57] Song I-H, Kwon I-M, Kim H-D, Kim Y-W. Processing of microcellular silicon carbide ceramics with a duplex pore structure. Journal of the European Ceramic Society. 2010;30:2671-6.

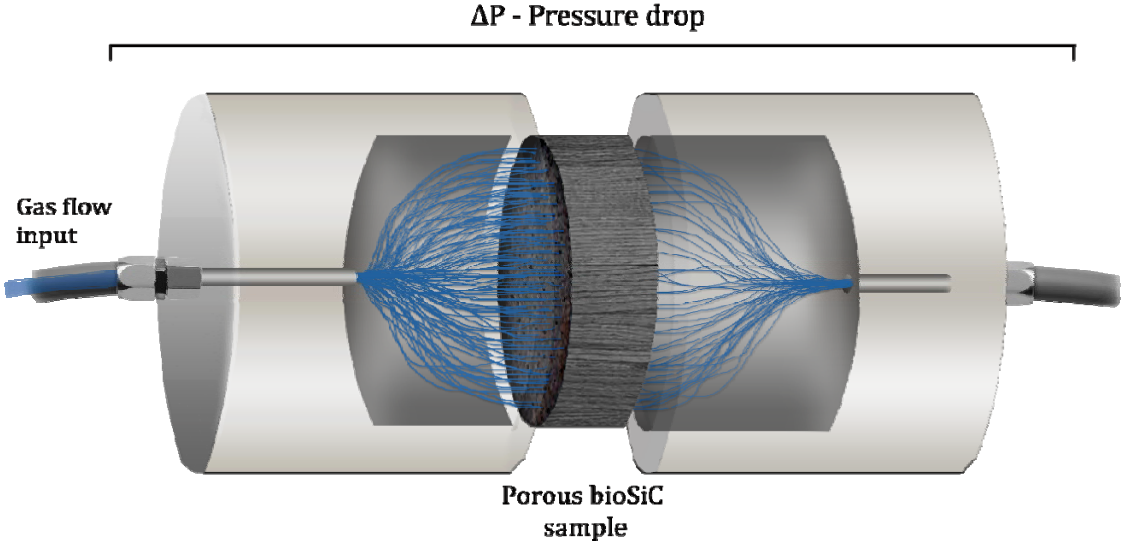
ΔP - Pressure drop
Gas flow input
Porous bioSiC sample

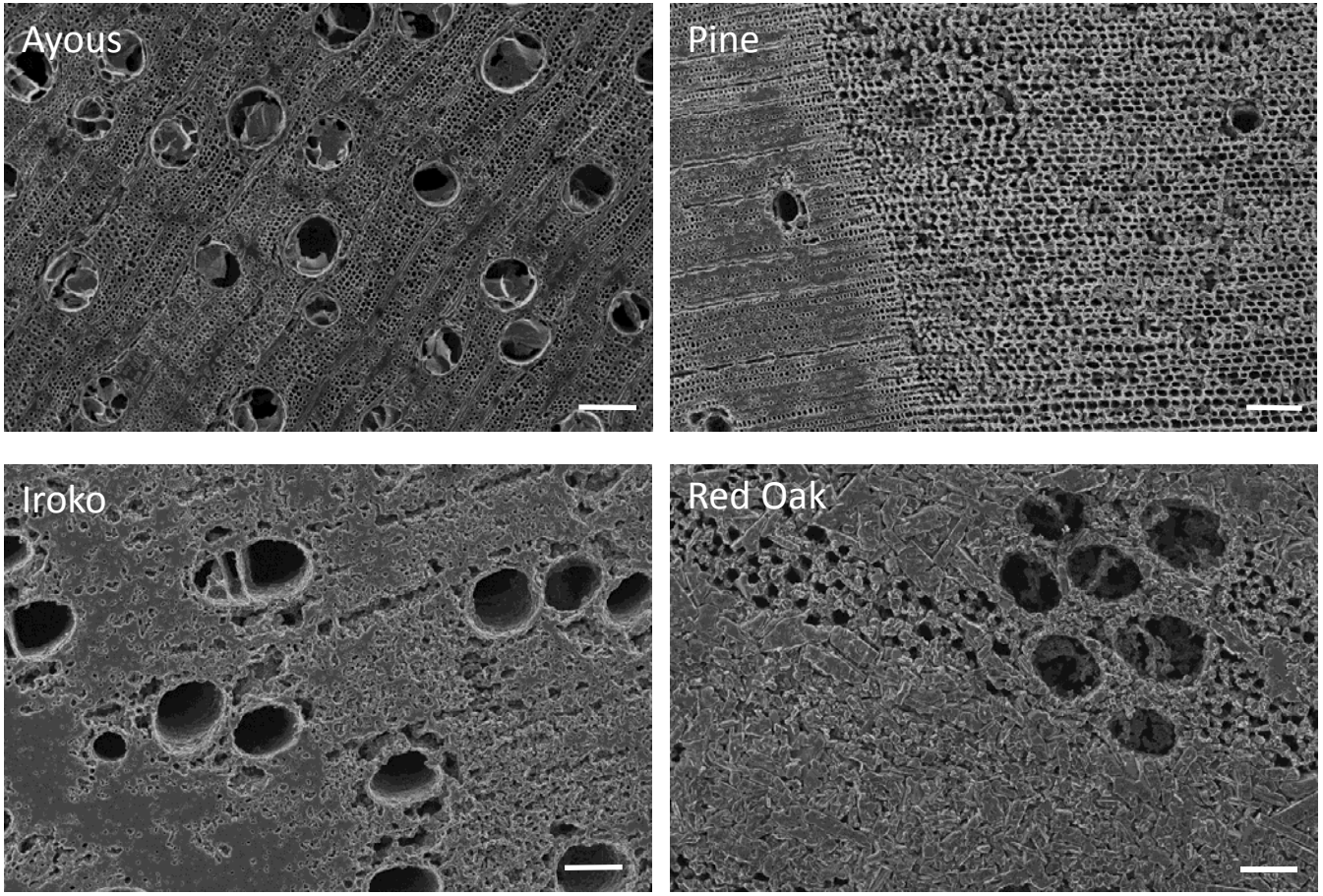
Ayous
Pine
Iroko
Red Oak

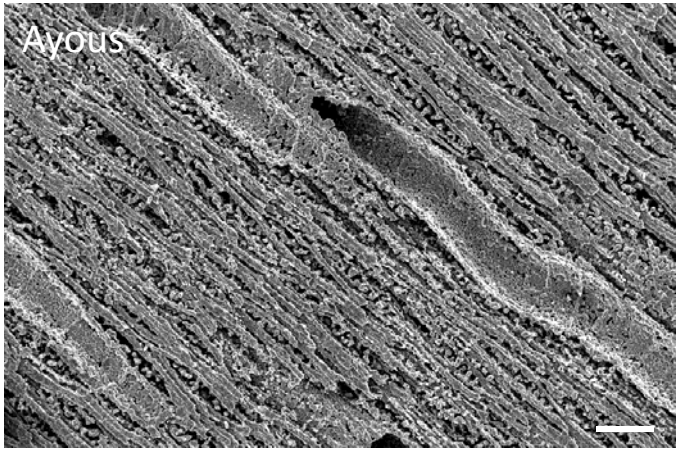
Ayous

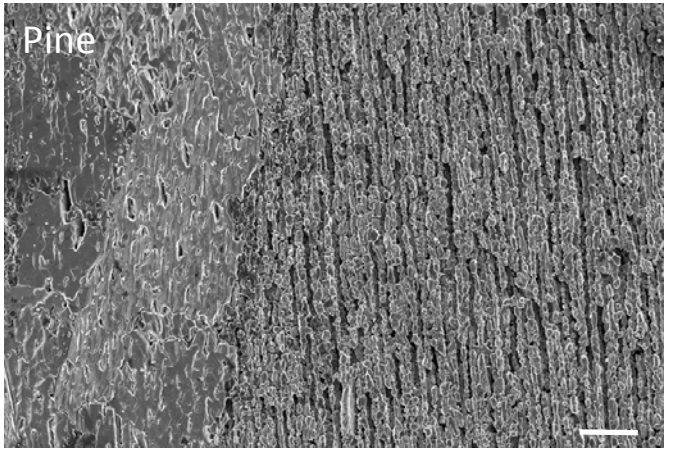
Pine

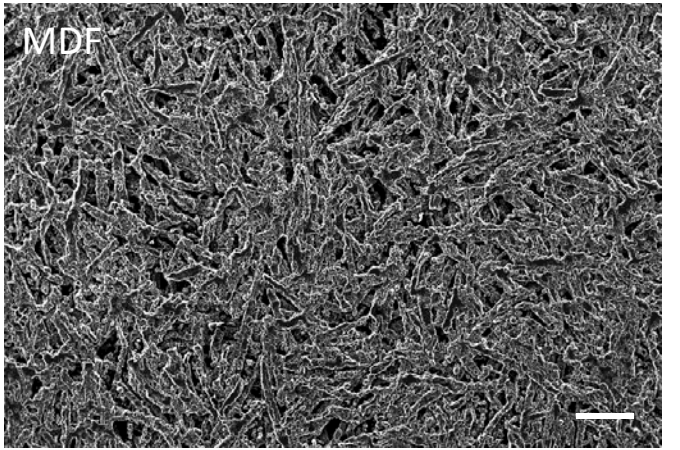
MDF

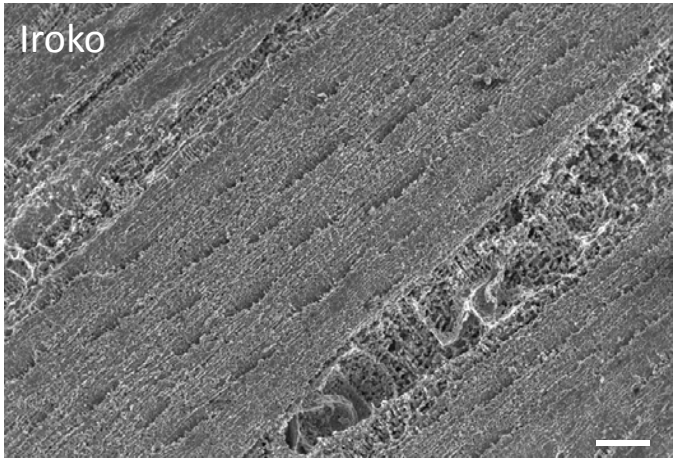
Iroko

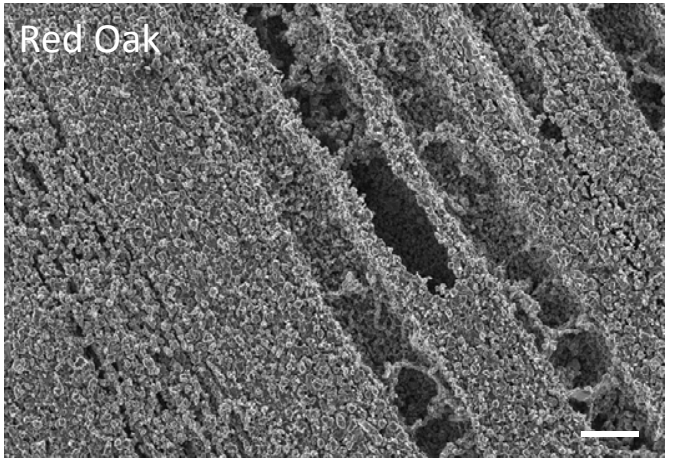
Red Oak

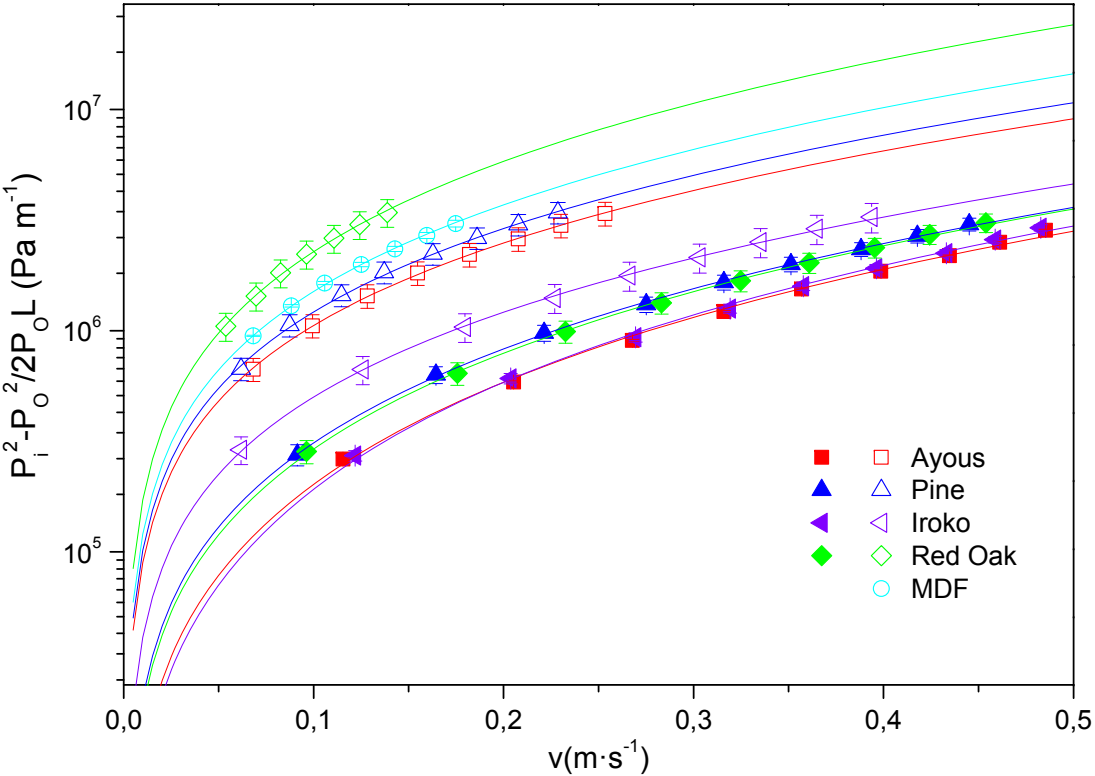
$P_i^2-P_O^2/2P_OL$ (Pa m^{-1})
10^7
10^6
10^5
0,0
0,1
0,2
0,3
0,4
0,5
v(m·s^{-1})
Ayous
Pine
Iroko
Red Oak
MDF

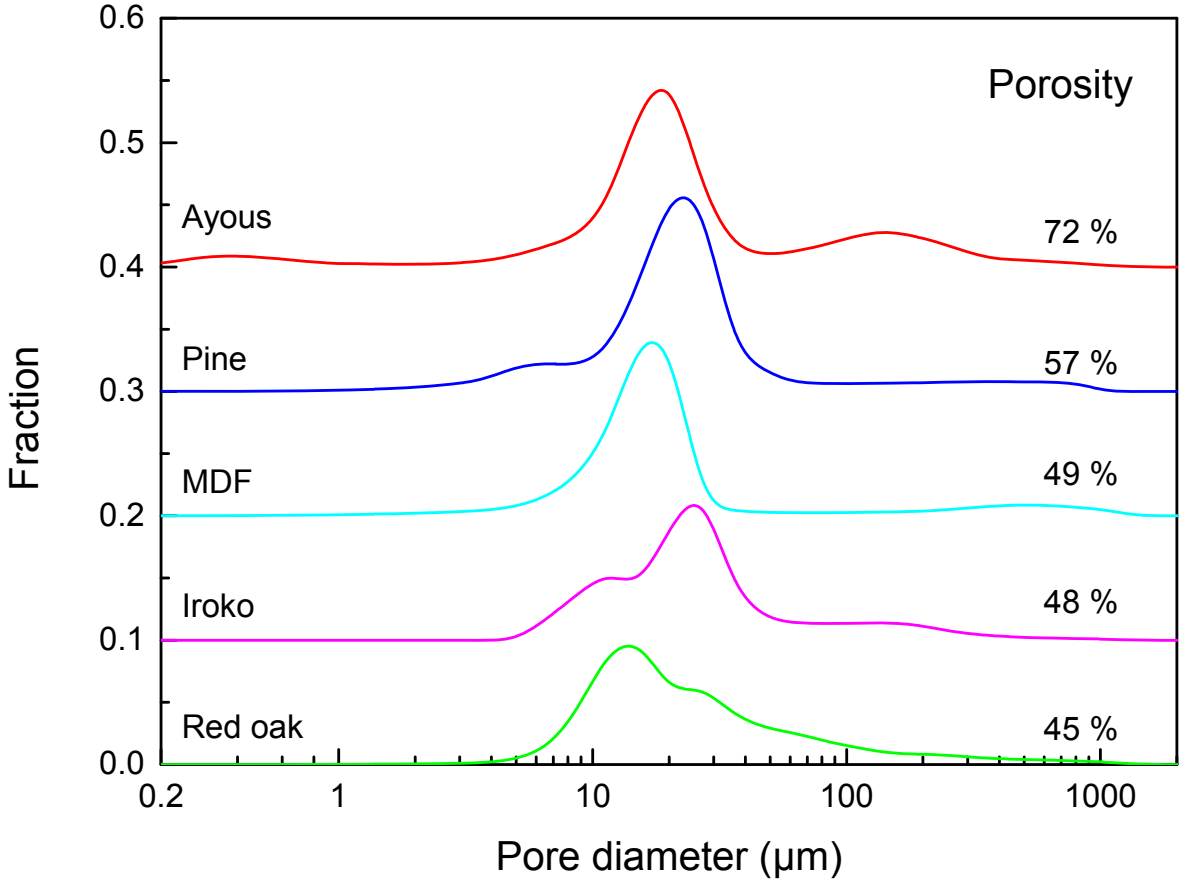
Porosity
Ayous
72 %
Pine
57 %
MDF
49 %
Iroko
48 %
Red oak
45 %
Fraction
Pore diameter (µm)
0.0
0.1
0.2
0.3
0.4
0.5
0.6
0.2
1
10
100
1000

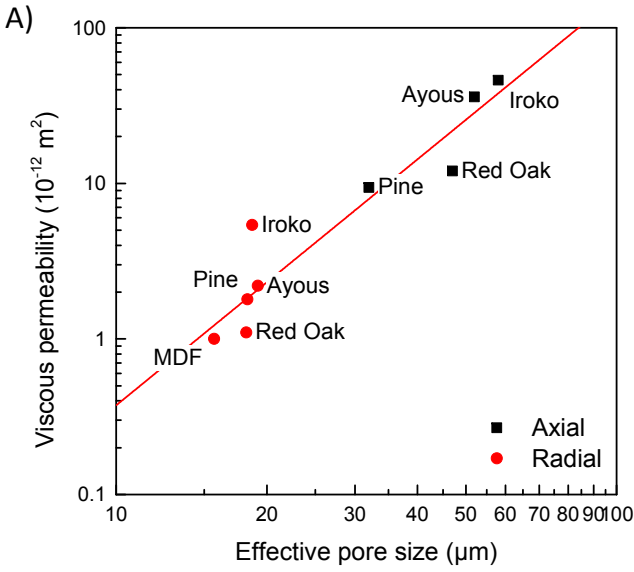
A)
Viscous permeability (10^{-12} m^2)
Effective pore size (μm)
100
10
1
0.1
10
20
30
40
50
60
70
80
90
100
Ayous
Iroko
Red Oak
Pine
Iroko
Pine
Ayous
Red Oak
MDF
Axial
Radial

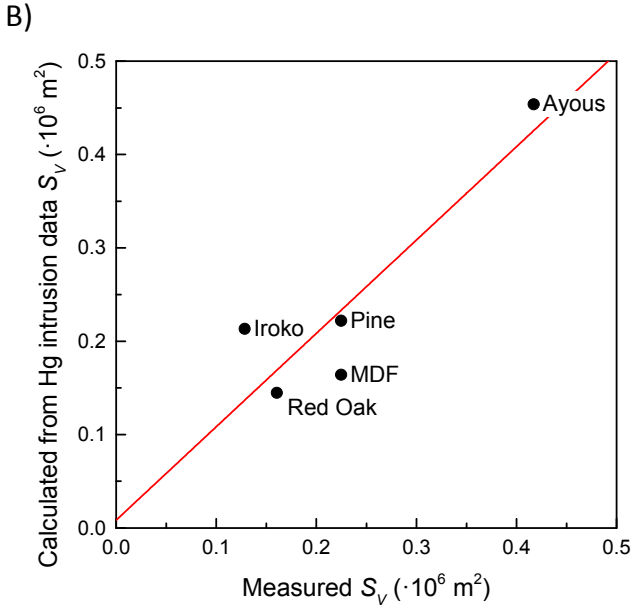
B)
Calculated from Hg intrusion data S_V ($\cdot 10^6$ m^2)
Measured S_V ($\cdot 10^6$ m^2)
0.5
0.4
0.3
0.2
0.1
0.0
0.0
0.1
0.2
0.3
0.4
0.5
Ayous
Iroko
Pine
MDF
Red Oak

A)

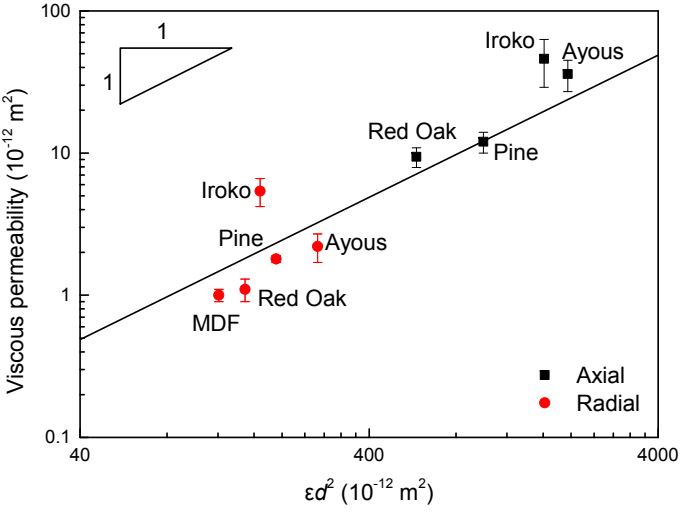
100
10
1
0.1
40
400
4000
1
1
Viscous permeability (10^{-12} m^2)
εd^2 (10^{-12} m^2)
Iroko
Ayous
Red Oak
Pine
Iroko
Pine
Ayous
Red Oak
MDF
Axial
Radial

B)

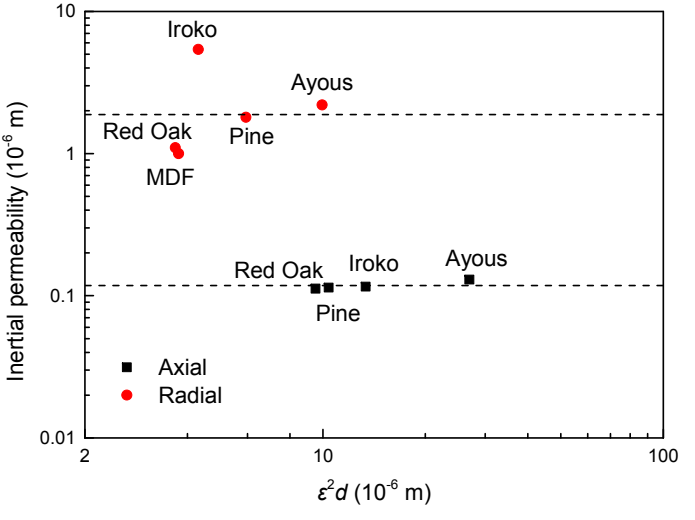
10
1
0.1
0.01
2
10
100
Inertial permeability (10^{-6} m)
$\varepsilon^2 d$ (10^{-6} m)
Iroko
Ayous
Red Oak
Pine
MDF
Red Oak
Iroko
Ayous
Pine
Axial
Radial

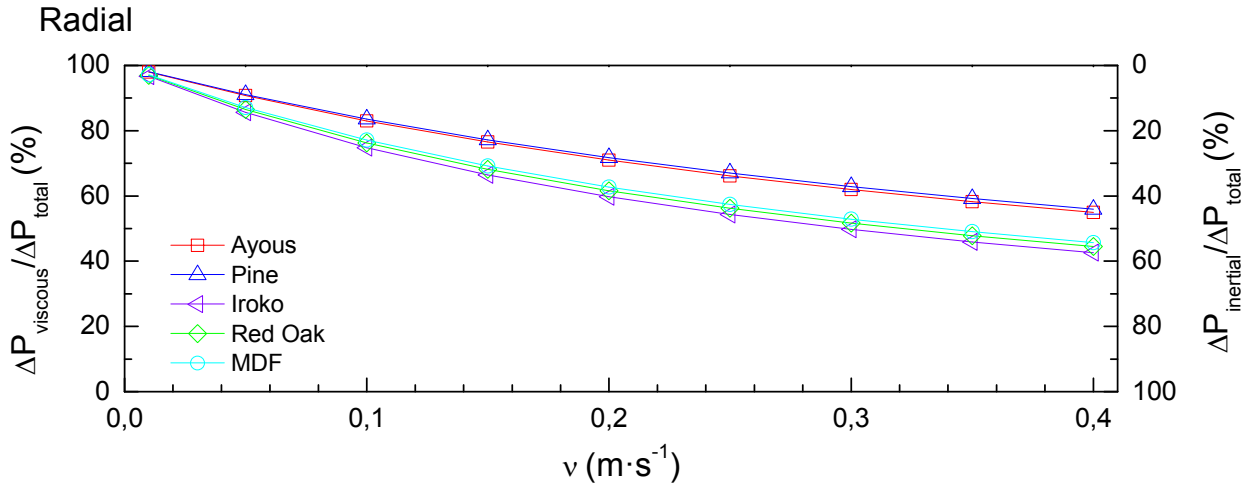
Radial
ΔP viscous /ΔP total (%)
ΔP inertial /ΔP total (%)
ν (m·s-1)
Ayous
Pine
Iroko
Red Oak
MDF
0
20
40
60
80
100
0,0
0,1
0,2
0,3
0,4

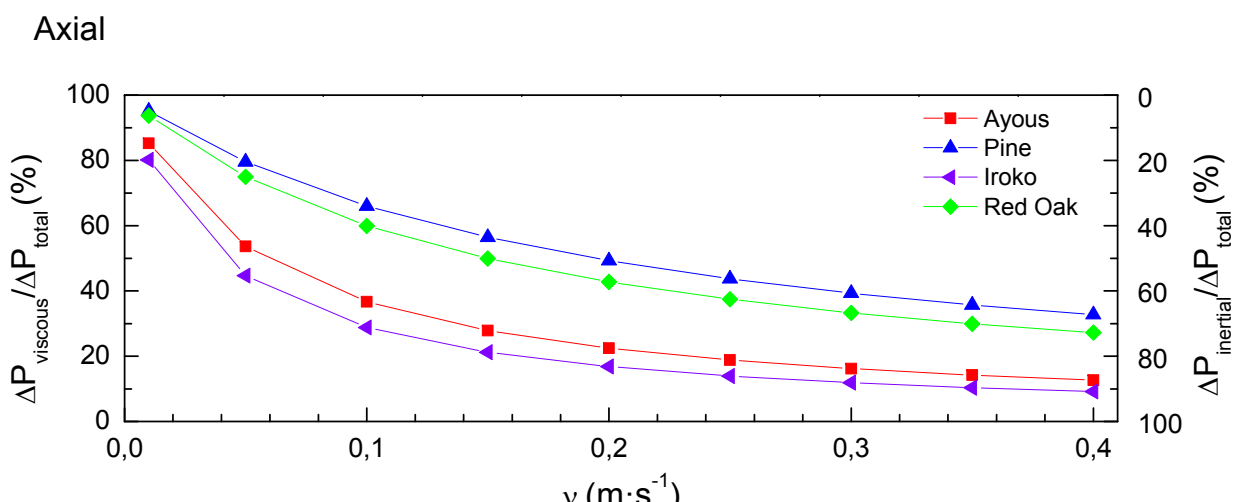
Axial
ΔP viscous /ΔP total (%)
ΔP inertial /ΔP total (%)
ν (m·s-1)
Ayous
Pine
Iroko
Red Oak
0
20
40
60
80
100
0,0
0,1
0,2
0,3
0,4

A)

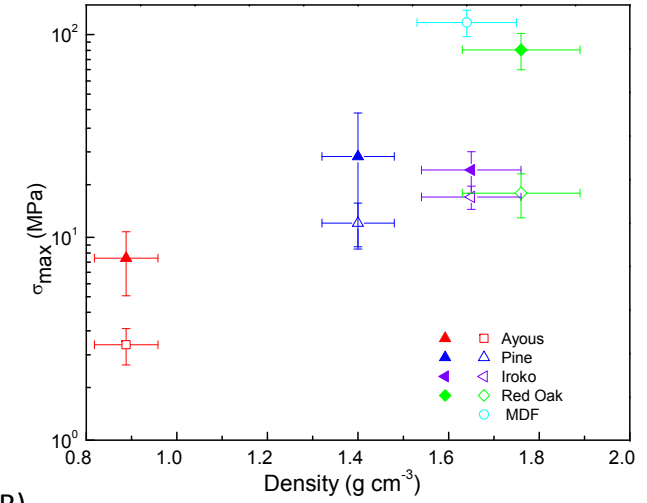
10^2
10^1
10^0
σ_{max} (MPa)
0.8
1.0
1.2
1.4
1.6
1.8
2.0
Density (g cm^{-3})
Ayous
Pine
Iroko
Red Oak
MDF

B)

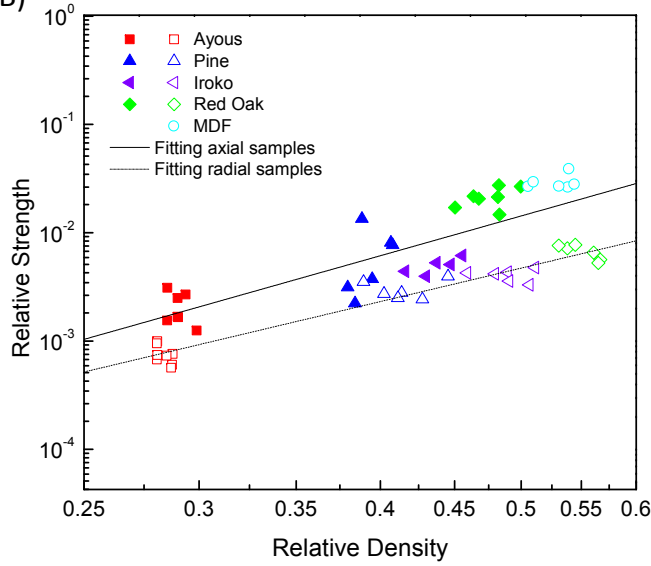
10^0
10^{-1}
10^{-2}
10^{-3}
10^{-4}
Relative Strength
0.25
0.3
0.35
0.4
0.45
0.5
0.55
0.6
Relative Density
Ayous
Pine
Iroko
Red Oak
MDF
Fitting axial samples
Fitting radial samples

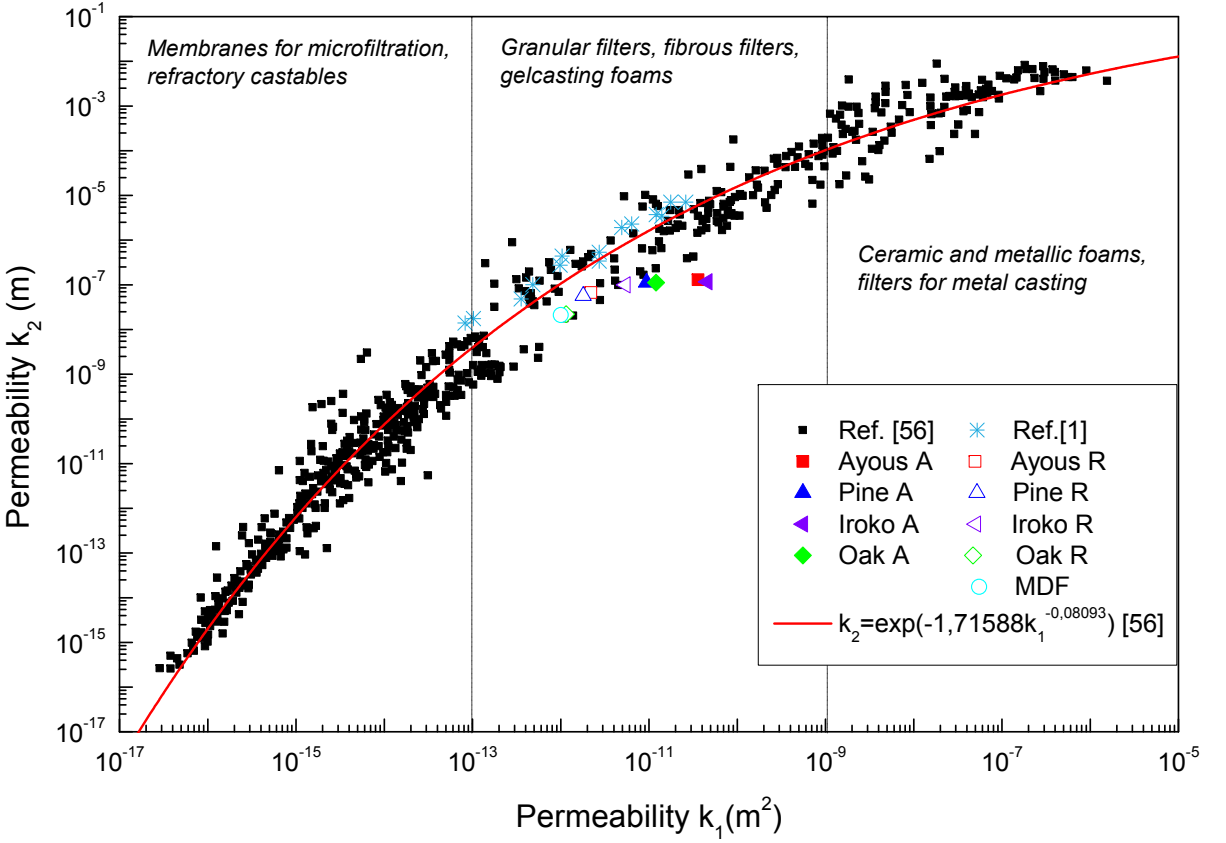
Membranes for microfiltration, refractory castables
Granular filters, fibrous filters, gelcasting foams
Ceramic and metallic foams, filters for metal casting
Ref. [56]
Ref.[1]
Ayous A
Ayous R
Pine A
Pine R
Iroko A
Iroko R
Oak A
Oak R
MDF
k2=exp(-1,71588k1-0,08093) [56]
Permeability k2 (m)
Permeability k1(m2)
10-1
10-3
10-5
10-7
10-9
10-11
10-13
10-15
10-17
10-17
10-15
10-13
10-11
10-9
10-7
10-5